Compare Results

Old File:

2D_analytical_AD_model_13-08-2023-org.pdf

34 pages (971 KB)
13-08-2023 09:02:30

versus

New File:

2D_analytical_AD_model__revised-19-10-2023.pdf

34 pages (987 KB)
19-10-2023 12:30:39

Total Changes

537

Content

146 Replacements

195 Insertions

173 Deletions

Styling and Annotations

15 Styling

8 Annotations

Go to First Change (page 1)

An analytical linear two-dimensional Actuator Disc Model and comparisons with CFD simulations

Helge Aagaard Madsen[1]

[1]DTU, Dept. of Wind and Energy Systems, Roskilde, Denmark

Correspondence: Helge Aagaard Madsen (hama@dtu.dk)

Abstract. The continuous upscaling of wind turbines enabled by more lightweight and flexible blades in combination with coning has challenged the assumptions of a plane disc in the commonly used BEM type aerodynamic codes for design and analysis of wind turbines. The objective with the present work is thus to take a step back relative to the integral 1-D momentum theory solution in the BEM model in order to study the AD flow in more details.

We present an analytical, linear solution for a two dimensional (2-D) AD flow with one equation for the axial velocity and for the lateral velocity, respectively. Although it is a 2-D model, we show in the paper that there is a good correlation with axis-symmetric and three-dimensional (3-D) CFD simulations on a circular disc. The 2-D model has thus the potential to form the basis for a simple and consistent rotor induction model.

For a constant loading, the axial velocity distribution at the disc is uniform as is the case of the classical momentum theory for an AD. However, an important observation of the simulated flow field is that immediately downstream of the disc the axial velocity profiles change rapidly to a shape with increased induction towards the edges of the disc and less induction on the central part. This is typically what is seen at the disc in full non-linear CFD AD simulations as we compare with in the paper. By a simple coordinate rotation the analytical solution is extended to a yawed disc with constant loading. Again, a comparison with CFD, now with a 3-D simulation on a circular disc in yaw, confirms a good performance of the analytical 2-D model for this more complicated flow.

Finally, a further extension of the model to simulate a coned disc is obtained using a simple superposition of the solution of two yawed discs with opposite yaw angles and positioned so the two discs just touch each other. Now the validation of the model is performed with results from axis-symmetric CFD simulations of an AD with a coning of 20 deg and -20 deg, respectively. In particular, for the disc coned in the downwind direction there is a very good correlation between the simulated normal velocity to the disc whereas some deviations are seen for the upwind coning.

The promising correlation of the results for the 2-D model in comparison with 3-D simulations of a circular disc with CFD for complicated inflow like what occurs at yaw and coning indicates that the 2-D model could form the basis for a new, consistent rotor induction model. The model should be applied along diagonal lines on a rotor and coupled to an angular momentum model. This application is sketched in the outlook and is subject for future research.

1 Nomenclature

a axial induction factor

a_l axial induction factor related to the $2D_l$ model

a_m axial induction factor in momentum theory

b half width of the 2-D actuator disc

c chord

C_d sectional drag coefficient

C_l sectional lift coefficient

C_Q rotor torque coefficient

C_T thrust coefficient

C_{Tl} thrust coefficient related to the $2D_l$ model

C_{Tm} thrust coefficient related to the momentum theory

C_x projection of C_l and C_d tangential to the rotor plane

C_y projection of C_l and C_d perpendicular to the rotor plane

f_x body force in x direction non-dimensional with ρV^3

f_y body force in y direction non-dimensional with ρV^3

g_x induced body force in x direction non-dimensional with ρV^3

g_y induced body force in x direction non-dimensional with ρV^3

p pressure non-dimensional with ρV^2

N_B number of blades

r radial position

T thrust

v_n normal velocity perpendicular to AD non-dimensional with V

v_t tangential induced velocity non-dimensional with V

v_x velocity component in x direction non-dimensional with V

v_y velocity component in y direction non-dimensional with V

V free stream velocity

V_r relative velocity at blade section

w_x induced velocity component in x direction non-dimensional with V

w_y induced velocity component in y direction non-dimensional with V

x, y, z space coordinates non-dimensional with b and with x in stream-wise direction

Greek letters

Δp pressure jump over the AD and non-dimensional with ρV^2

ρ air density

φ inflow angle

Θ yaw angle

ξ, η, ζ supplementary space coordinates non-dimensional with b and ξ perpendicular to the AD and η along the width of the AD

Abbreviations

AD Actuator Disc

AD_l Linear solution for the AD flow

AC Actuator Cylinder

AS Actuator Surface

BEM Blade Element Momentum

CFD Computational Fluid Dynamics

2 Introduction

The most striking characteristic of the modern, industrial wind turbine development over the last 4-5 decades is the up-scaling. In the beginning of the eighties there was already an industrial series production of turbines with a rated power of 50-100 kW and rotor diameters of 15-20 m. Many were installed in big wind farms like Palm Springs and Tehachapi in US. Today turbines of the maximum size of around 15 MW with rotor diameters of 230-240 m are introduced on the market which gives an up-scaling factor of around 15 on rotor diameter over this time span.

It's clear that this up-scaling correspondingly increased the requirements to the aerodynamic and aeroelastic design tools like the modelling of unsteady inflow over the rotor disc, wind shear and wind veer, yawed flow, wake flow, [Madsen et al. (2020)]. The origin of the aerodynamic modelling of the common aeroelastic models tools today like (FLEX5 (Flex4) (Øye, 1996), FAST (Jonkman et al., 2016), BLADED (Bossanyi, 2003), GAST (Riziotis and Voustinas, 1997), Cp-Lambda (Botasso and Croce, 2006-2013), FOCUS (WMC, 2019), HAWC2 (Larsen and Hansen, 2007)) is the Blade Element Momentum (BEM) theory based on the propeller theory by Glauert (1935) which originally assumed homogeneous and stationary flow. Various modifications have been implemented in the different codes to adapt to the conditions mentioned above. Most codes e.g. now use a more local representation of the induction over the rotor plane than on a ring element as originally proposed, to better account for varying inflow over the rotor disc from wind shear and turbulence.

An excellent overview of the capability of most of the above mentioned codes has recently been presented by Boorsma et al. (2023). This was done by both bench-marking and validation to experimental data as well as to higher fidelity model data. One conclusion is that the BEM type codes still show higher deviations for yawed inflow than higher fidelity codes like CFD and vortex type codes. For yawed flow cases the variability between BEM type codes is the double of the variability between CFD codes. This illustrates lack of a unified implementation of the sub models in BEM type codes, e.g. for the modelling of yaw.

The objective with the present work is thus to take a step back relative to the integral momentum theory solution for an actuator disc which is the core in the BEM model. We will study the AD flow in more details to provide a better background for understanding of the shortcomings and approximations in the BEM implemented momentum theory and deviations from higher fidelity modelling of AD flow such as: 1) the velocity distribution at the disc for constant loading; 2) independence of annular stream tubes; 3) flow field for a yawed AD and 4) flow field for a coned AD.

With respect to the axial velocity distribution for a constant loaded AD where the integral momentum theory predicts (assumes) a uniform, constant profile, a number of CFD based AD simulations have shown higher induction towards the edges of the disc and less induction on the central part, (Sørensen and Kock, 1995), (Madsen, H. A., 1997), (Mikkelsen et al., 2001). Also the shortcomings of the momentum theory to predict the flow through a coned rotor have been illustrated by CFD AD simulations of Madsen and Rasmussen (1999) and Mikkelsen et al. (2001) where considerable deviations from the constant axial velocity profile assumed by the momentum theory are found.

Studies within these four areas have been carried out by many researchers in the past and it seems that the modelling can be grouped into three approaches; 1) vortex models; 2) combined analytical/numerical models and 3) Euler equation based models which the present model belongs to.

The approach based on vortex models is by far the most common way of studying the AD flow field and not least the use of a the vortex cylinder (VC) model with a none-expanding wake; infinite number of blades; infinite tip speed ratio and uniform loading. Some recent studies in relation to the above mentioned research areas using this model are Branlard and Gaunaa (2015) (relations between momentum theory and vortex theory), Li et al. (2022) (modelling of non-planar rotors), Troldborg et al. (2014) (yawed disc) and Gaunaa et al. (2023) (independence of annular stream tubes).

In the category of studies combining analytical and numerical solutions Crawford (2006) presented a modified BEM for coned rotors. The improvement of the BEM model comprises a proper consideration of the relative placement of the wake and including the radial induced velocity. A comparison of the improved BEM with the CFD results of (Madsen, 2000) and (Mikkelsen et al., 2001) shows reasonable correlation as concerns the slope of the profiles on the inner part of the disc whereas the non-linear outboard part required a further modelling of the expansion of the stream tubes.

Another study by van Kuik and Lignarolo (2016) shows the non-uniformity of the axial velocity profile caused by the pressure acting at the stream tube annuli and thus making them not independent from each other in contradiction to the independence found by Gaunaa et al. (2023). Finally in this group of models can be mentioned the work by Wood and Hammam (2022) who used conservation of axial and angular momentum and the calculus of variations to derive the optimal performance of horizontal-axis wind turbines over a wide range of tip speed ratio. In the 2-D model to be presented here the analytical solution is limited to a constant loading.

In the third model group, the Euler equations and the continuity equation together with specified body forces are the starting point for modelling the AD flow. It seems to be a unique approach and only the so-called asymptotic acceleration potential method by van Bussel (1992) has some resemblance with the method used in the present research.

It might be considered surprising to study a 2-D AD model for representation of rotor induction. However, it's expected that the main difference between an axis-symmetric and a 2-D model will be related to analogy between radial velocity and lateral velocity for the axis-symmetric and 2-D model, respectively, where the last mentioned is expected to have highest velocities. The model and the background for its derivation is presented in Section 3 followed by flow characteristics of the AD model in axial flow in Section 4 including comparisons with axis-symmetric CFD simulations. Section 5 extends the model to yawed inflow and the validation with 3-D CFD AD simulations. Section 6 presents a further extension for modelling a coned disc and comparisons with axis-symmetric CFD AD simulation of a disc with 20^o and -20^o coning, respectively. Outlook and conclusions are given in Section 7 and Section 8, respectively.

3 The analytical 2-D AD model

The analytical linear solution $2D_l$ for the AD model was first presented by Madsen (1983) during a work on development of the Actuator Cylinder (AC) model for modelling the aerodynamics of vertical axis wind turbines (VAWTs). The basic idea behind the AC model was the need to extend the well-known Actuator Disc concept to an Actuator Surface (AS) of arbitrary shape where the AS coincides with the swept surface of the considered turbine type, Madsen (1983), Madsen (1985), Madsen (1988). For a straight bladed VAWT rotor this means a cylindrical shape which thus can be modelled with the AC model. However, this extension of the AD concept to an AS raised the question of how to compute the flow field through and around an AS. The well-known momentum theory solution on integral form for an AD cannot just be transferred for use on an AS of arbitrary shape which would violate the assumptions in the AD momentum model.

3.1 Derivation of the describing equations

We have chosen an approach for derivation of the equations that follows a general method of Von Kármán and Burgers (1935) for analysis of flow fields with a main velocity V under influence of external body forces f. Karman and Burgers used the method to develop a general theory for wings of finite span and considered in most cases the induced velocities from the action of external forces as perturbations to the main flow field with the velocity V.

Koning (1935) presented an analysis of the flow around "the ideal propeller" described as a thin disc with axial forces acting over the disc, which is based on the method of Von Kármán and Burgers (1935) and thus also forms the basis for the present work. However, Koning studied the axis-symmetric flow problem, where we here will stick to a two-dimensional (2-D) flow. The reason to focus on the 2-D flow case is that, as we will see later, a complete and simple analytical solution can be derived, which gives valuable and relevant insight into different flow features whereas Koning for the analysis of the axis-symmetric case had to introduce approximations or assumptions, e.g. that the pressure solution found along the center line of the disc was assumed to be valid at other radial positions. As we also will see later, the 2-D AD flow has characteristics resembling the 3-D AD flow and thus the potential to form the basis for a wind turbine rotor induction model. Furthermore the simple approach to model a coned rotor with two yawed disc is a big advantage for the 2-D model.

It should be noted that the full 3-D set of equations for the flow around an arbitrary three-dimensional AS has been presented by Madsen (1985) and Madsen (1988).

3.1.1 The full non-linear 2-D solution

The approach for derivation of the describing equations is based on the Euler equations on differential form and the equation of continuity with the external body forces f specified on the AD. Assuming steady flow the 2-D Euler equations take the form:

$$v_x \frac{\partial v_x}{\partial x} + v_y \frac{\partial v_x}{\partial y} = -\frac{1}{\rho}\frac{\partial p}{\partial x} + \frac{1}{\rho} f_x \tag{1}$$

$$v_x \frac{\partial v_y}{\partial x} + v_y \frac{\partial v_y}{\partial y} = -\frac{1}{\rho}\frac{\partial p}{\partial y} + \frac{1}{\rho} f_y \tag{2}$$

and the equation of continuity:

$$\frac{\partial v_x}{\partial x} + \frac{\partial v_y}{\partial y} = 0. \tag{3}$$

Following the approach by Von Kármán and Burgers (1935) we rewrite the velocity components as:

$$v_x = V + w_x \tag{4}$$

$$v_y = w_y. \tag{5}$$

Here V is the velocity of the main, uniform flow field; w_x, w_y the induced velocities by the action of the body forces and v_x,v_y the final velocity components.
We then non-dimensionalize the velocity components with V, the pressure p with $V^2\rho$ and volume forces f_x, f_y with $V^3\rho$. However, although we now have non-dimensionalized the equations, the notation of velocity, body force components and pressure will not be changed.
Inserting the new velocity components notation and the non-dimensionalization in Eqs. 1,2 and 3 and rearranging we get:

$$\frac{\partial w_x}{\partial x} = -\frac{\partial p}{\partial x} + f_x - \left(w_x \frac{\partial w_x}{\partial x} + w_y \frac{\partial w_x}{\partial y} \right) \tag{6}$$

$$\frac{\partial w_y}{\partial x} = -\frac{\partial p}{\partial y} + f_y - \left(w_x \frac{\partial w_y}{\partial x} + w_y \frac{\partial w_y}{\partial y} \right) \tag{7}$$

and the continuity equation:

$$\frac{\partial w_x}{\partial x} + \frac{\partial w_y}{\partial y} = 0. \tag{8}$$

Following the terminology of Kármán and Burgers, the terms in the brackets on the right hand side of Eq. 6 and 7 can be interpreted as induced or second order forces g_x, g_y defined as:

$$g_x = -\left(w_x \frac{\partial w_x}{\partial x} + w_y \frac{\partial w_x}{\partial y}\right), \tag{9}$$

$$g_y = -\left(w_x \frac{\partial w_y}{\partial x} + w_y \frac{\partial w_y}{\partial y}\right). \tag{10}$$

Inserting Eq. 9 and10 into Eq. 6, 7 we get:

$$\frac{\partial w_x}{\partial x} = -\frac{\partial p}{\partial x} + f_x + g_x, \tag{11}$$

$$\frac{\partial w_y}{\partial x} = -\frac{\partial p}{\partial y} + f_y + g_y. \tag{12}$$

Now we take the divergence of Eq. 11 and 12:

$$\frac{\partial^2 w_x}{\partial x^2} = -\frac{\partial^2 p}{\partial x^2} + \frac{\partial f_x}{\partial x} + \frac{\partial g_x}{\partial x}, \tag{13}$$

$$\frac{\partial^2 w_y}{\partial x \partial y} = -\frac{\partial^2 p}{\partial x \partial y} + \frac{\partial f_y}{\partial y} + \frac{\partial g_y}{\partial y}. \tag{14}$$

Differentiating the equation of continuity Eq. 8 with respect to x and inserting we get:

$$\frac{\partial^2 p}{\partial x^2} + \frac{\partial^2 p}{\partial y^2} = \left(\frac{\partial f_x}{\partial x} + \frac{\partial f_y}{\partial y}\right) + \left(\frac{\partial g_x}{\partial x} + \frac{\partial g_y}{\partial y}\right). \tag{15}$$

This is the type of Poisson's equation and with the boundary conditions that the body forces are zero at infinity the solution takes the form:

$$p(f) = \frac{1}{2\pi} \iint \frac{f_x(x-\xi) + f_y(y-\eta)}{(x-\xi)^2 + (y-\eta)^2} d\xi d\eta \tag{16}$$

and the pressure part from the g terms:

$$p(g) = \frac{1}{2\pi} \iint \frac{g_x(x-\xi) + g_y(y-\eta)}{(x-\xi)^2 + (y-\eta)^2} d\xi d\eta. \quad (17)$$

The pressure for the full solution can then the be written as:

$$p = p(f) + p(g). \quad (18)$$

This shows that the full solution for the pressure is derived as the sum of two parts. One part, the linear part, being a function of the prescribed forces f on the disc and the non-linear part, which is a function of the g forces called second order or induced forces.

When the pressure is derived the velocity components can be determined by integration of Eq. 11 and Eq. 12.

We will now in the remaining part of the paper focus on the linear solution of the AD flow as this part is much simpler than the full solution. This is because the f forces are prescribed and only different from zero on the disc whereas the g forces are different from zero in the whole wake region. See Von Kármán and Burgers (1935) for more details.

Furthermore, it is important to notice that the linear solution is still a valid solution satisfying the equations, however for a new flow problem where also the g forces, derived on basis of the linear solution, have to be considered as external body forces. The evaluation and interpretation of the linear solution with this in mind is valuable for understanding the flow characteristics of the linear AD flow solution.

This insight into the linear solution is also the basis for the procedure for deriving the full non-linear solution in an iterative manner, see Von Kármán and Burgers (1935). In a first iteration the derived g forces from the linear solution are inserted as volume forces but with opposite sign. Then a new solution, which now is a function of both the f and g forces, is derived comprising the solution of the Poisson equation over the area where the g forces are acting. This iterative solution procedure continues until the solution don't change from iteration to iteration. The technique has been used for the solution of the full non-linear AC flow model, Madsen (1983).

3.2 The analytical linear (2D$_l$) solution for the 2-D disc

In the linear solution the flow field is only acted upon by the body forces f on the infinitely thin actuator disc as the induced body forces g are assumed to be zero (see Fig.1 for notation). The pressure field is then derived from Eq. 15 which now has the form:

$$\frac{\partial^2 p}{\partial x^2} + \frac{\partial^2 p}{\partial y^2} = 0. \quad (19)$$

This is the Laplace equation. The pressure p will thus be a potential function outside the disc showing a jump Δp over the disc. Following the derivation by Koning (1935) the potential function for the pressure can be obtained by covering the surface with doublets with strength Δp. The pressure jump Δp is linked to the body forces f_x as:

$$\Delta p(\eta) = \int\limits_S d\eta \lim_{\epsilon \to 0} \int\limits_{-\epsilon}^{\epsilon} f_x d\xi. \tag{20}$$

As mentioned above Koning (1935) derived the solution for an axis-symmetric disc but we will derive the pressure potential for a 2-D disc or in fact an actuator strip with a width of $2b$ and extending from $-z$ to z and with doublets with the intensity Δp distributed over the surface S. For any point not situated on the disc the potential will according to Koning (1935) be given by:

$$p = \frac{1}{4\pi} \int\limits_S \Delta p \frac{\partial}{\partial n} (\frac{1}{\omega}) dS \tag{21}$$

where n denotes the positive normal to the disc and ω the distance from any point on the disc to the point A where the potential is calculated.

The details of the derivation can be found in Appendix A.

The resulting pressure function has been derived to:

$$p = -\frac{1}{2\pi} \int\limits_{-1}^{1} \Delta p \frac{x}{x^2 + (y-\eta)^2} d\eta \tag{22}$$

where x, y have been non-dimensionalised with the half width b of the disc.

The induced axial velocity w_x can now be found integrating Eq. 11 from $-\infty$ to x:

$$w_x = -p + \int\limits_{\infty}^{x} f_x d\xi = \frac{1}{2\pi} \int\limits_{-1}^{1} \Delta p \frac{x}{x^2 + (y-\eta)^2} d\eta + \Delta p \qquad \text{(last term only in the wake, } x > 0\text{).} \tag{23}$$

The w_y component is determined through Eq. 12 with $f_y = 0$. It means first differentiating p with respect to y and then integrating $\partial p / \partial y$ from $-\infty$ to x. The derivation found in Appendix B leads to the following equation for w_y:

$$w_y = \int\limits_{\infty}^{x} \frac{\partial p}{\partial y} d\xi = \frac{1}{2\pi} \int\limits_{-1}^{1} \Delta p \frac{y - \eta}{x^2 + (y-\eta)^2} d\eta. \tag{24}$$

3.2.1 The analytical linear 2D$_l$ solution for a constant disc loading

With a constant loading Δp on the disc, the pressure and velocity components can be derived by integrating the Eqs. 22, 23, 24 over the width of the disc. The derivation of the pressure function shown in Appendix C leads to:

$$p = -\frac{1}{2\pi}\Delta p[\arctan\frac{(1-y)}{x} + \arctan\frac{(1+y)}{x}] \quad (25)$$

$$(26)$$

and then inserting the pressure equation in Eq. 23 we get:

$$w_x = \frac{1}{2\pi}\Delta p[\arctan\frac{(1-y)}{x} + \arctan\frac{(1+y)}{x}] + \Delta p \qquad \text{(last term only in the wake, } x > 0\text{).} \quad (27)$$

Likewise the integration of w_y for constant loading, shown in Appendix D yields:

$$w_y = \frac{\Delta p}{4\pi}\ln\left(\frac{x^2+(y+1)^2}{x^2+(y-1)^2}\right). \quad (28)$$

Finally, according to Eq. 4 the v_x, v_y velocity components are derived as:

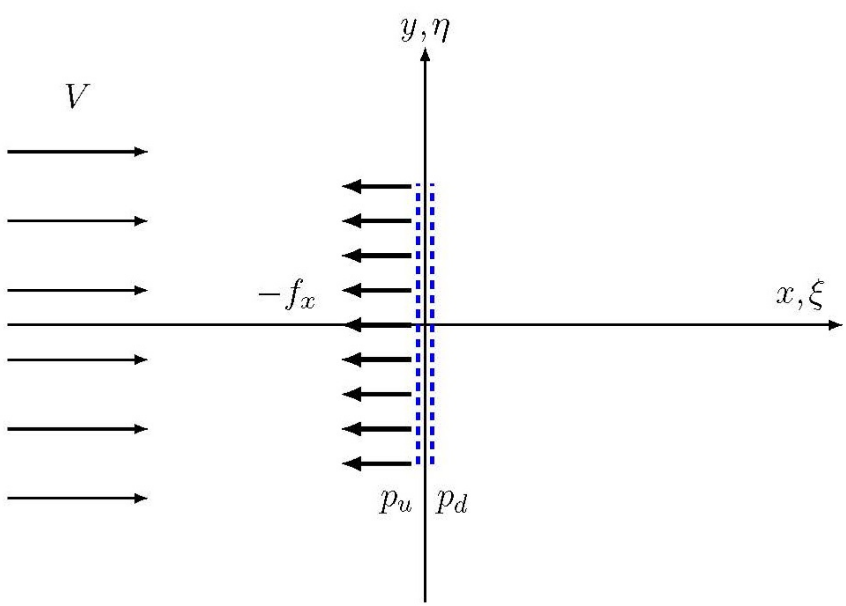

Figure 1. Notation for the 2-D actuator disc.

$$v_x = 1 + w_x, \quad (29)$$

$$v_y = w_y. \quad (30)$$

4 AD flow characteristics

In this section we will study the flow characteristics through the 2-D actuator disc by numerical exploration based on the analytical linear solution, $2\mathrm{D}_l$, for a constant, uniform loading of the disc.

First we relate the pressure jump, Δp, to the thrust, T, and thrust coefficient, C_T:

$$T = 2b\Delta p, \tag{31}$$

where $2b$ is the width of the actuator disc.

From the definition of the thrust coefficient, C_T, we get:

$$C_T = \frac{T}{2b\frac{1}{2}\rho V^2}. \tag{32}$$

Combining equations 31 and 32 and keeping in mind that Δp is non-dimensionalized with ρV^2 we get:

$$C_T = 2\Delta p. \tag{33}$$

4.1 Velocity profiles v_x, v_y

For a loading corresponding to a thrust coefficient $C_T = 0.4$ the v_x and v_y velocity profiles as function of y are shown for different up-stream and down-stream positions in Fig. 2. The v_x velocity profiles are seen to develop from a Gaussian type profile upstream the disc to be sharper when approaching the disc and finally at the disc be completely rectangular with with free stream velocity just outside the disc. Accelerated flow above free stream velocity is then seen to occur just downstream the disc and peaking before $x = 2$. Further downstream in the wake the velocity profiles become almost rectangular at $x = 10$ and with a deficit within the projected area of the disc which means a non-expanding wake.

The v_y profiles are seen to be anti-symmetric around the x-axis as expected and have a strong peak at the edge of the disc. Downstream the profiles decay fast.

The momentum solution for the v_x component, also shown in Fig. 2, is seen to be lower than the actual linear solution which will be explored next.

4.2 Scaling C_T to fit the $2D_l$ solution to momentum theory

As seen above the $2D_l$ solution does not fit exactly with the classical momentum theory solution for an actuator disc. The computed induction is lower and it is an important shortcoming for wider use of the model as a rotor induction model.

To investigate that further we derive the relation between the thrust coefficient C_{Tl} of the $2D_l$ model and the induction coefficient, a_l, for the $2D_l$ solution presented above.

The axial velocity v_{xd} at the disc is derived from Eq. 28 by $x \to -0$:

$$w_{xd} = \frac{\Delta p}{2\pi}\left(\frac{\pi}{2} + \frac{\pi}{2}\right) = \frac{\Delta p}{2} \tag{34}$$

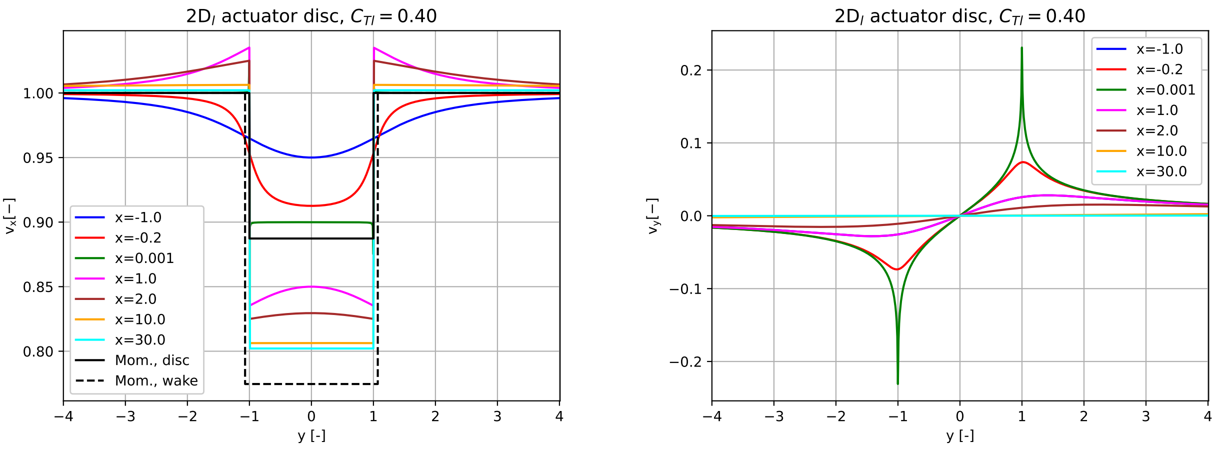

Figure 2. In the left graph the axial velocity component $v_x$is shown as function of the lateral coordinate y for different stream wise positions x from upstream the disc to far downstream in the wake for a thrust coefficient of 0.4. The velocity profiles for the momentum solution are also shown at the disc and in the far wake, respectively. In the right graph the lateral velocity component v_y is shown for the same positions.

and from the definition of a:

$$a_l = 1 - v_{xd} = 1 - (1 - w_{xd}), \tag{35}$$

$$a_l = w_{xd} = \frac{\Delta p}{2} = \frac{C_{Tl}}{4}, \tag{36}$$

or

$$C_{Tl} = 4a_l \tag{37}$$

The classical momentum theory derived as an axis-symmetric solution for a circular actuator disc gives the following relation between the thrust coefficient, C_Tm, and the induction, a_m, (the subscript m to denote momentum theory):

$$C_{Tm} = 4a_m(1 - a_m). \tag{38}$$

Comparing the solution from the two models, the momentum theory gives a velocity at the disc, $v_{xm} = 0.887$, for a C_T of 0.4 while the ADl model gives $v_x = 0.9$ for a similar C_T.

The reduced induction by the AD_l model is due to the action of the induced body forces defined in Eq. 9 and Eq. 10 that accelerate the flow in the wake regions $y > -1$ and $y < 1$ and also through the disc and upstream the disc through the pressure field from the g forces.

Without a detailed derivation of the g forces we can conclude that there will be g_x forces along the lines, $y = \pm 1$, in the wake region responsible for acceleration of the flow through the disc requiring increased external volume forces, f_x, (increased C_{Tl}) in order to correlate with the velocity at the disc from the momentum solution. A check of the x-momentum balance of a control volume around the disc in some distance will show that the balance is only full-filled if the g forces are considered as external body forces. This has been demonstrated for the AC flow models based on the same solution approach (Madsen, 1982)

The analogy to use a fixed wake vortex model for the same flow problem would be a vortex sheet along the lines $y = \pm 1$. This vortex sheet will require external body forces to be fixed (non-expanding wake) because the flow in the vicinity of the disc is not aligned with the vortex sheet and thus induces forces on the sheet.

In order to force the $2D_l$ model to give the same induction in the rotor plane and in the far field wake as the momentum theory we can simply scale the thrust coefficient based on Eqs. 37 and 38:

$$\frac{C_{Tl}}{C_{T_m}} = \frac{4a_l}{4a_m(1-a_m)}, \tag{39}$$

$$\tag{40}$$

and enforcing a_l to be equal to a_m we get:

$$C_{Tl} = C_{T_m}\frac{4a_m}{4a_m(1-a_m)} = C_{T_m}\frac{1}{1-a_m}. \tag{41}$$

(Futher down we will denote C_{Tm} as C_T).

For example for a thrust coefficient of 0.89 we shall increase C_{Tl} to 1.34 to match the momentum solution as shown in the left graph in Fig. 3. As mentioned above this considerable increase in C_T is necessary due to the strong impact of the g forces on the wake flow which is seen clearly in the right graph in Fig. 3. Here the v_x velocity profiles together with the enclosing streamlines of the disc show that part of the flow passing through the disc and thus de-accelerated due to the f forces at the disc plane is accelerated up to free stream velocity shortly down in the wake region. Although the g forces are only acting from the disc plane and downstream along the lines $y = \pm 1$ the pressure field from these forces will also influence the flow upstream the disc.

It can finally be noticed that the same scaling procedure for correcting a linear solution is used in the Actuator Cylinder model for the VAWT´s implemented in HAWC2. However, in this case the correction is applied directly as scaling of the velocity components, Madsen et al. (2013).

4.3 Superposition of solutions for more discs

As we have a linear model type we can easily study interaction of more discs with e.g. different loading or location to each other. Later we will show that the superposition is one way to model a coned disc by the superposition of two yawed discs.

Let a new disc 2 have the origin x_{D2}, y_{D2} and a loading Δp_{D2} in the original coordinate system as shown in Fig. 1. We get then the contributions v_{xD2}, v_{yD2} to the velocity field by inserting into Eq. 27 and Eq. 28:

$$w_{xD2} = \frac{1}{2\pi}\Delta p_{D2}[\arctan\frac{1-(y-y_{D2})}{x-x_{D2}} + \arctan\frac{1+(y-y_{D2})}{x-x_{D2}}] + \Delta p_{D2} \qquad \text{(last term only in the wake of disc 2)}, \tag{42}$$

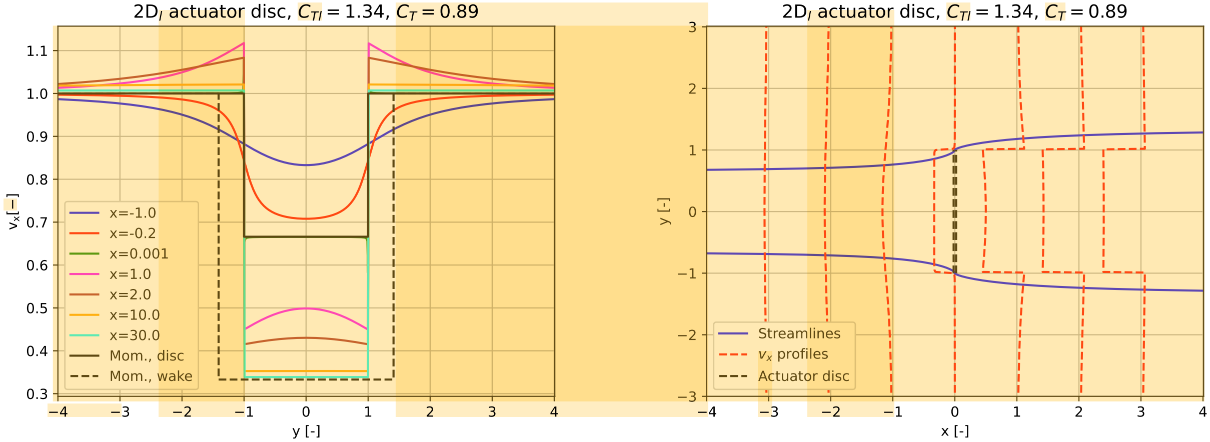

Figure 3. In the left graph the axial velocity component v_x is shown as function of the lateral coordinate y for different stream wise positions x from upstream the disc to far downstream in the wake for a thrust coefficient of 1.34 in the $2D_l$ model and compared with the momentum solution for a C_T of 0.89. In the right graph the enclosing streamlines of the disc for the same loading are shown together with v_x profiles at different streamwise positions. The streamlines are derived on basis of the local flow angle $\arctan(\frac{v_y}{v_x})$ with starting points at the edge of the disc.

$$w_{yD2} = \frac{\Delta p_{D2}}{4\pi} \ln\left(\frac{(x-x_{D2})^2 + ((y-y_{D2})+1)^2}{(x-x_{D2})^2 + ((y-y_{D2})-1)^2}\right). \tag{43}$$

However, the set-up does not work for overlapping discs.

Here the superposition will first be used to study an important characteristic of the model for discs at the same streamwise position with different loadings as is the example in the left part of Fig. 4. The discs are positioned so close that they form one disc with double width, $4b$, and with a thrust coefficient of 0.89 and 0.45, on each half part, respectively. Upstream and downstream the discs there is a clear interaction between the v_x velocity profiles of the discs but exactly in the plane of the discs there is no interaction of the axial velocity component although the thrust coefficient jumps from 0.89 on the lower part to the half, 0.445, on the upper part.

This can be used to guide the implementation of BEM model in aerodynamic and aeroelastic codes as proposed by Gaunaa et al. (2023) using a VC model on a similar case. The result justifies a local, point-wise evaluation of the momentum balance, e.g. used in the implementation of the BEM model in the HAWC2 code. Finally, it should be noticed that there is an interaction of the lateral velocity component in the disc plane.

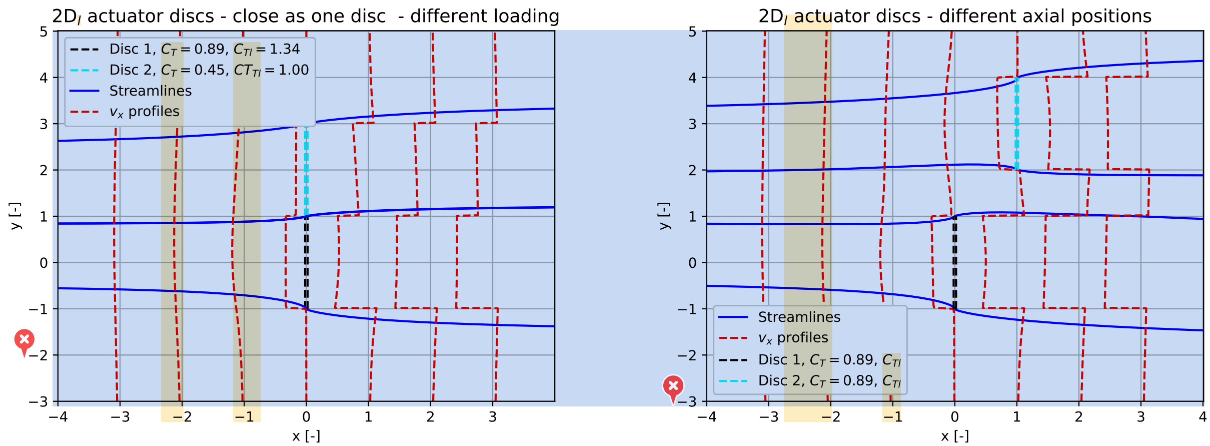

Figure 4. In the left graph we show the flow characteristics of two discs placed side by side so they just touch. The lower disc has the double loading of the upper disc. Enclosing streamlines for the two discs are shown together with v_x velocity profiles at different axial positions. To the right the same type of data are shown, however for the same loading on the two discs and with disc no. 2 shifted a distance of half the disc width in both x and y direction.

When the two discs do not have the same streamwise position we see an interaction of the v_x profiles as is the case in the example in the right part of Fig. 4. A slightly increased induction can be seen on the upper part of disc 1. Furthermore, an accelerated axial flow velocity between the two discs is noted.

4.4 An important characteristic of the velocity profiles of the 2D$_l$ model at a small distance downstream the disc and comparison with CFD simulations

In Fig. 3 we saw that at the disc and far downstream in the wake the v_x profiles were rectangular but in between some bending or curved profiles could be seen, e.g. at $x = 1$ and $x = 2$. We will now go much closer to the disc where we find the development of the profiles as shown in the left graph in Fig. 5. It's clearly seen that the v_x velocity profiles immediately develop from a uniform distribution to shapes with stronger deceleration close to $y = \pm 1$. The same is typically seen in full, non-linear simulations of AD flow, (Sørensen and Kock, 1995), (Madsen, H. A., 1997) and (Mikkelsen et al., 2001). We use here the results of Madsen and Rasmussen (1999) from an axis-symmetric simulation of an AD. Comparing the axial velocity profile at the disc from the CFD simulation with profiles from the 2D$_l$ model extracted at different downstream positions we find the best correlation in shape using the 2D$_l$ profiles at $x = 0.08$ and scaled with a factor 1.05 as shown in the right graph of Fig. 5.

The reason for this development of the v_x profiles close behind the disc is probably that in this region the g forces along the lines $y = \pm 1$ are acting both upstream and downstream the axial position where we extract the velocity profiles. Therefore, there might be some local cancelling of their influence so that the deficit is closer to the full solution. The left graph of Fig.

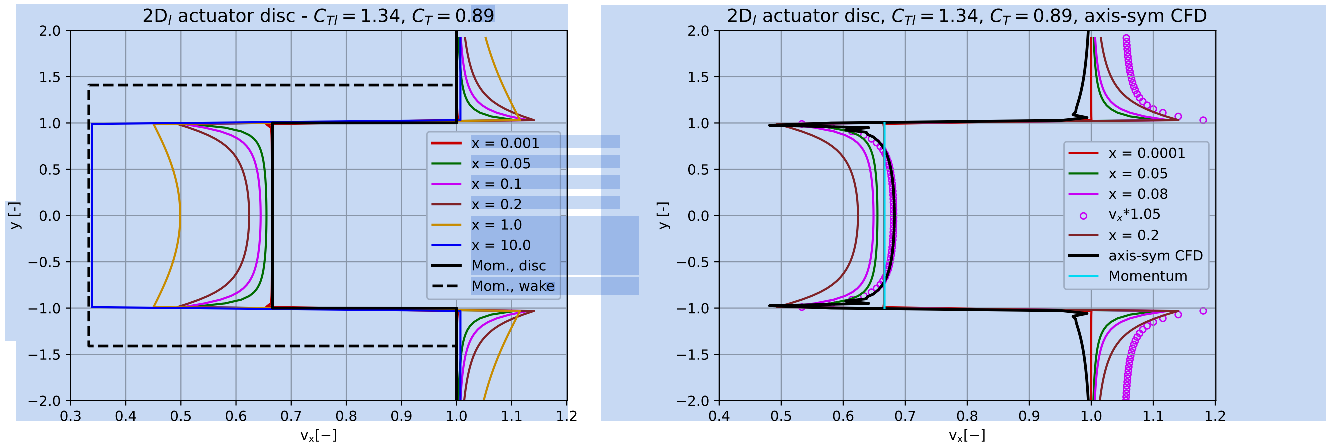

Figure 5. In the left graph we show the axial velocity v_x profiles at positions close behind the disc as well as further downstream for a thrust coefficient of 0.89. For comparison the momentum solution for v_x at the disc and in the far wake is also included. In the graph to the right the v_x velocity profile at the disc from an axis-symmetric CFD AD simulation is compared with the 2D$_l$ profile at a downstream distance of 0.08 scaled with factor 1.05 to account for the decrease of velocity downstream behind the disc and to give the best fit to the CFD results extracted at the disc.

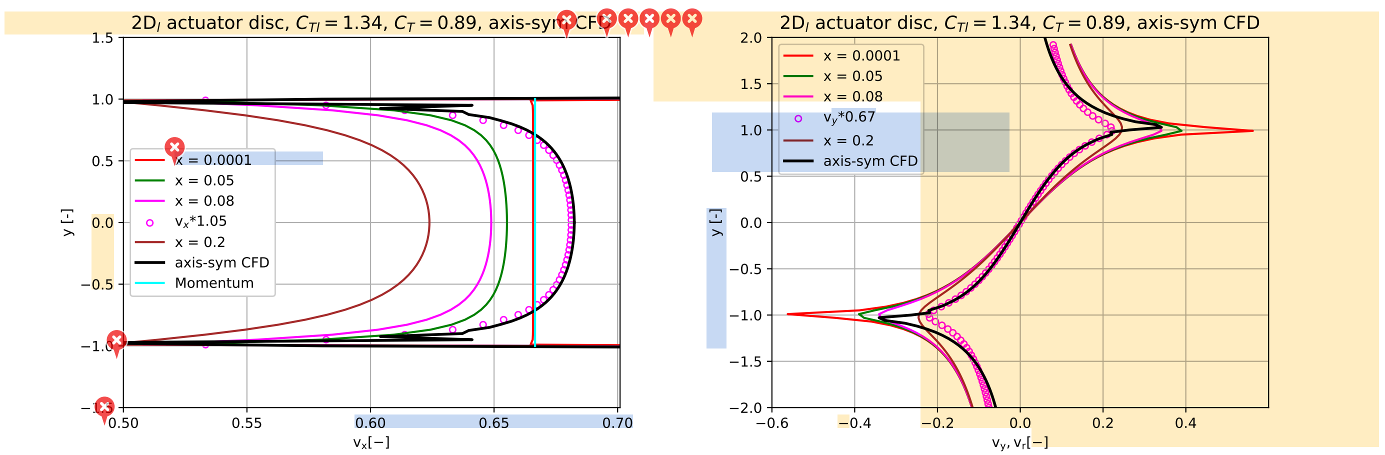

Figure 6. The graph to the left is a zoom of the right graph in Fig. 5. In the right graph 2D$_l$ v_y velocity profiles are compared with the radial velocity profile from an axis-symmetric simulation. At the same downstream position $x = 0.08$ as for the v_x component the best fit for v_y is obtained with a scaling factor of 0.67.

6 shows a very good correlation with the CFD solution, when applying the above scaling. It is expected that such scaling is necessary as we have computed the velocity profile a short distance downstream of the disc where the axial velocity decays

rapidly. For a wider application of the 2D$_l$ model it is important that the scaling factor is constant. Therefore, we will use the same scaling in the remaning flow examples in the paper.

Finally, the v_y profiles are compared with the profiles of the radial velocity component, v_r, from CFD simulations in the right graph of Fig. 6. When v_y is computed at the same position, $x = 0.08$, as for v_x the best fit is obtained scaling down with a factor, 0.67. The need for a strong down-scaling is expected as a 2-D solution will have a much stronger lateral velocity component than the radial velocity in an axis-symmetric solution.

5 The 2D$_l$ solution for yawed flow and comparisons with 3-D AD CFD computations with constant loading

We continue now to derive the analytical solution for a 2-D AD in yawed flow, see Figure 7. This is an important flow situation for a turbine which causes increased loading and reduced power. However, yaw is now frequently studied and used for wake steering in wind farms to increase the power of downstream turbines by upstream wake deflection.

The objectives with the present model derivation is a further study of the capability of the simple model to handle complex flow like a yawed AD. Further the objective is in a next step (next section) to combine two yawed discs with opposite yaw angles to model a coned rotor.

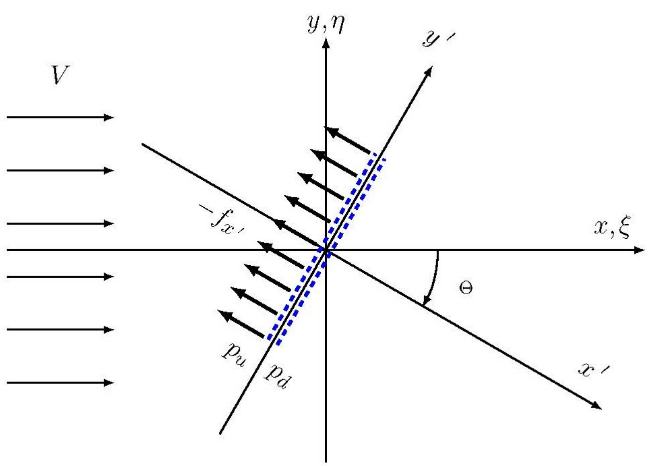

Figure 7. Notation for the 2-D actuator disc in yaw.

The starting point is the flow solution for w_x and w_y in Eqs. 27, 28 in the non-yawed x, y coordinated system which then is rotated by the yaw angle, Θ, into the new system, $x\prime, y\prime$, see Figure 7. The velocity components, w_x and w_y, in the original system, x, y, are then derived as function of $x\prime, y\prime$.

The following coordinate transformation is introduced:

$$x' = (x\cos\Theta - y\sin\Theta), \tag{44}$$

$$y' = (x\sin\Theta + y\cos\Theta). \tag{45}$$

The coordinate transformations are inserted into eq. 27, 28:

$$w_x = \frac{\Delta p}{2\pi}\left(\arctan\frac{1-(x\sin\Theta + y\cos\Theta)}{x\cos\Theta - y\sin\Theta} + \arctan\frac{1+(x\sin\Theta + y\cos\Theta)}{x\cos\Theta - y\sin\Theta}\right), \tag{46}$$

and

$$w_y = \frac{\Delta p}{4\pi}\ln\left(\frac{(x\cos\Theta - y\sin\Theta)^2 + ((x\sin\Theta + y\cos\Theta)+1)^2}{(x\cos\Theta - y\sin\Theta)^2 + ((x\sin\Theta + y\cos\Theta)-1)^2}\right) \tag{47}$$

The total velocity components, v_x and v_y, for the yawed disc in the x,y coordinate system are then derived as:

$$v_x = 1 + w_x - \Delta p \qquad \text{(last term only in the wake of the yawed disc: } x' > 0 \text{ AND } y' > -\cos\Theta \text{ AND } y' < \cos\Theta\text{,}$$

$$v_y = w_y. \tag{48}$$

5.1 Streamlines and velocity profiles for a yawed disc of 30^o, 45^o and 60^o, respectively in comparison with 3-D CFD computations

We will now explore the flow field of a yawed disc of 30^o,45^o and 60^o, respectively, by presenting enclosing stream lines of the disc and axial velocity profiles from upstream to downstream positions, left graph in Figs. 8, 9 and 10. Further, a comparison with 3-D CFD AD simulations by Madsen (2001), Madsen et al. (2020) are shown in the graphs to the right.

We compare the normal velocity to the disc v_n along a line yd in a distance of $\Delta x = 0.08$ (see the streamline plots where the yd line is included) which was the distance we found above to give the best correlation with CFD for aligned flow. The normal velocity v_n to the disc is important as it is the velocity component in a rotor simulation with major influence on the angle of attack AoA.

We also show v_n along other lines parallel to the disc at other distances Δx where one is at the disc and one most downstream at $\Delta x = 0.2$. This is to illustrate the variation of the velocity profiles close behind the disc.

Starting with evaluation of the results for the yaw case of 30^o in Fig. 8 we find overall a very good correlation for the v_n profiles with considerable higher induction on the downstream edge of the disc. Also the non-linear shape in this region fits well with the CFD results. Similar non-linear velocity profiles are seen in the CFD simulations by Troldborg et al. (2014) and by the skewed cylindrical vortex wake model by Branlard and Gaunaa (2015).

Typically in engineering yaw modelling in aerodynamic and aeroelastic codes this velocity distribution is approximated with a linear correlation using the Glauert (1935) model as e.g. in the implementation in the HAWC2 code, (Madsen et al., 2020). We further notice the acceleration of v_n on the downstream edge of the disc and outside which is stronger than in the CFD results. This can mainly can be ascribed to the difference between a 2-D and 3-D flow solution with higher lateral velocities in the 2-D flow.

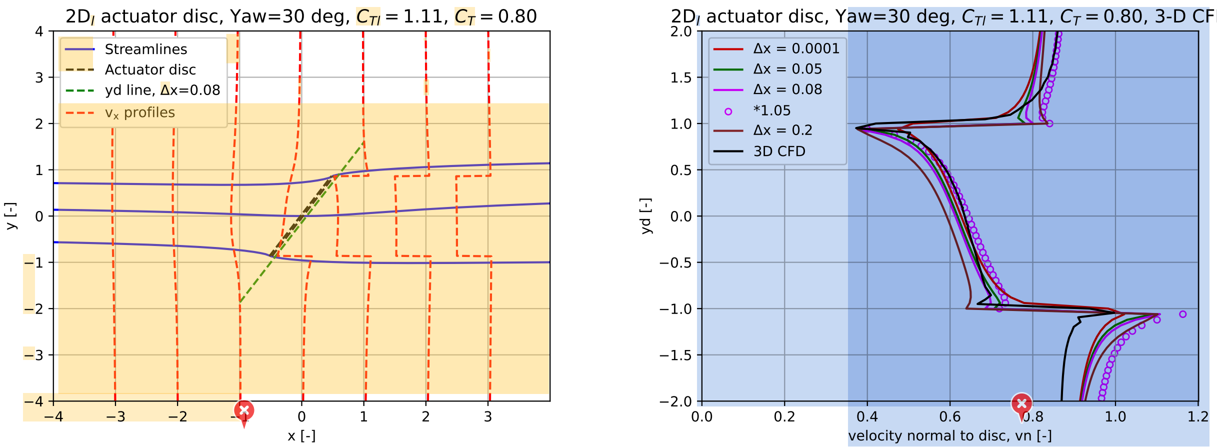

Figure 8. The left graph shows the enclosing streamlines of the yawed disc plus the streamline through the center of the disc for a yaw of 30^o, respectively. Further v_x profiles are shown at three x positions. We show also the line yd along the disc in a distance of $\Delta x = 0.08$ which is the line along which the normal velocity to the disc is shown in the right figure in comparison with 3-D CFD simulation of the AD.

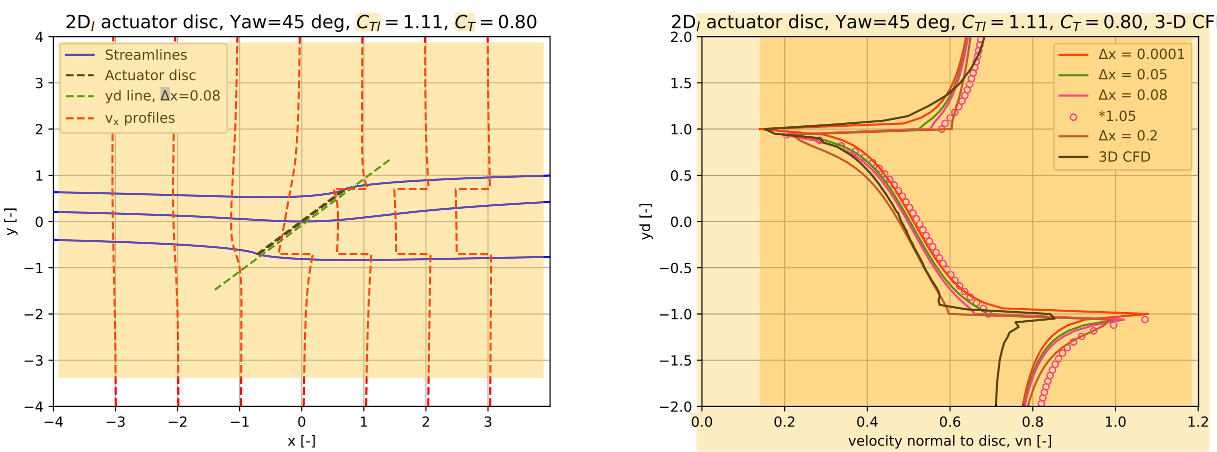

Figure 9. Similar graphs as in Fig 8 above but for a yaw of 45^o.

Continuing with the 45^o yaw case in Fig. 9 there is still overall a good correlation between the 2D$_l$ model results and the CFD computations. As above the correlation is almost perfect on the upstream half part of the disc whereas the deviations now are slightly increased on the other half part where the 2D$_l$ model computes less induction than the CFD results. Again this is probably due to the 2-D modelling of the flow that results in a stronger acceleration of the lateral flow, in particular outside the disc but now also influencing part of the flow through the disc close to the edge of the disc.

Finally to the 60^o yaw case in Fig. 10 we now see major deviations although the slope of the v_n curves is comparable. Overall the 2D$_l$ model computes less induction over the whole disc and this might be due to the scaling of C_T based on aligned flow where the wake with the g forces now is offset considerably from one side of the disc to the other.

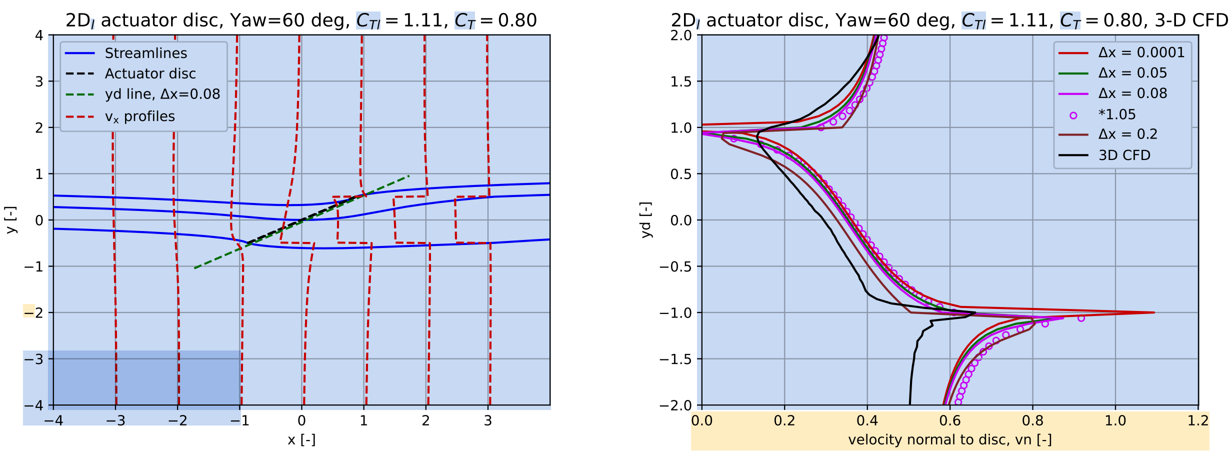

Figure 10. Similar graphs as in Fig 8 above but for a yaw of 60^o.

Based on the above comparison cases with 3-D CFD results we can conclude that 2D$_l$ model simulates yawed flow cases up to $30^o - 40^o$ with quite good resemblance and include details, like the bending of the v_n curves, not modelled by common engineering yaw models.

6 Modelling of coned rotors with the 2D$_l$ model

Modelling of coned rotors has been of big importance for decades in the wind research community as turbine concept studies often have included downwind coned rotors. This is due to potential advantages by such concepts by alleviating the flapwise blade root moment due to the deloading by centrifugal forces on a coned rotor or blade. In fact the CFD computations on coned rotors, (Madsen and Rasmussen, 1999), to be used here for comparisons were carried out back in time to provide input for design of a small two-bladed rotor (Vølund and Rasmussen, 1999) that could be coned up to 90^o for surviving storm situations. Recent concept studies that include downwind coned rotors are e.g. Bortolotti et al. (2019), Pao et al. (2021) and Bortolotti et al. (2022). These studies still rely on BEM type simulation tools which do not model any impact on induction from the coning which is in contrast to results with higher fidelity models like the CFD AD simulations presented here.

6.1 Modelling a coned disc by superposition of two yawed discs

The modeling of the coned rotor is based on the superposition of two yawed discs with an opposite yaw angle of $+-30^o$ as in the example shown in the left graph of Fig. 11. In this case there is still a distance between the edges of the discs and we can notice an accelerated flow between the discs.
However, when we now move the discs so close that the two edges just coincide as shown in the right graph of Fig. 11 we see one velocity deficit behind the two yawed discs and we can call it one coned disc with a cone angle of 30^o and the double size of the two yawed discs.

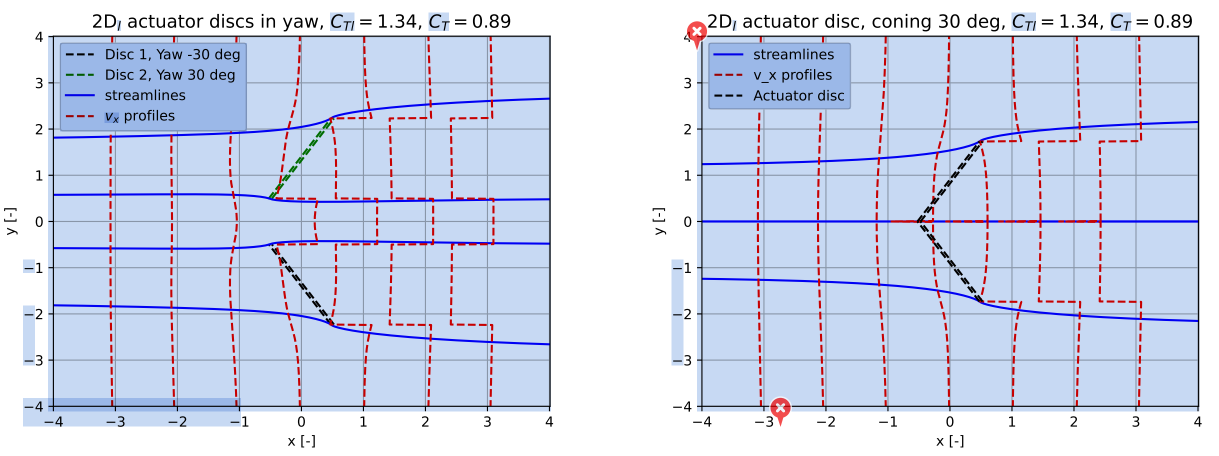

Figure 11. In the left graph we show two separated actuator discs with a yaw angle of 30^o and -30^o, respectively. In the right graph they are moved towards each other so the edges just coincide and form one coned disc of 30^o coning.

6.2 Comparison of the $2D_l$ with an axis-symmetric CFD simulation for a coned disc of 20^o and -20^o, respectively

Next we compare the $2D_l$ solution for a coned rotor with axis-symmetric CFD simulations as shown in the right graph of Fig. 12. As for the yawed disc we compare v_n as this is the most important velocity component in a rotor simulation with direct influence on angle of attack..

To be consistent with the distance behind the disc where we extract the $2D_l$ velocities, as tuned for aligned flow we use the same relative distance behind the disc which means in a double absolute distance $\Delta x = 2 \cdot 0.08$ as the coned disc has the double size of the aligned and yawed disc.
Comparing now the $2D_l$ simulations with the CFD results we see a very close correlation and just a small underestimation of v_n when using the data extracted at $\Delta x = 2 \cdot 0.08$. An almost complete coincidence is seen for the data extracted slightly closer

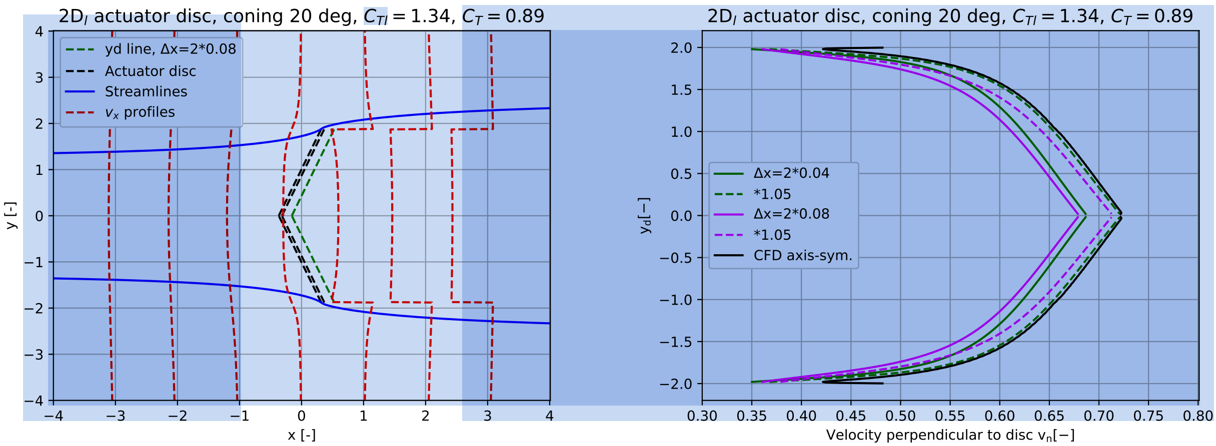

Figure 12. In the left graph we show the enclosing streamlines of a coned disc with 20^o coning and a $C_T = 0.89$. In the same graph we also show the y_d line parallel with the two disc parts in a distance of $\Delta x = 2 \cdot 0.08$ which are the lines along which we extract the velocities in the $2D_l$ model for comparison with the CFD results in the right graph. However, the CFD velocities were extracted at the disc.

to the disc at $\Delta x = 2 \cdot 0.04$.

In Fig. 13 we compare next the $2D_l$ simulations with CFD results for a cone angle of -20^o. First of all we notice that the shape of the curves are quite different from the velocity profiles for down wind coning as shown above as there is a decrease of the velocity close to the edge. However, the $2D_l$ model predict this quite well. The difference occurs when we apply the scaling of the velocities as it shifts the profile slightly towards higher velocities than the CFD results show.

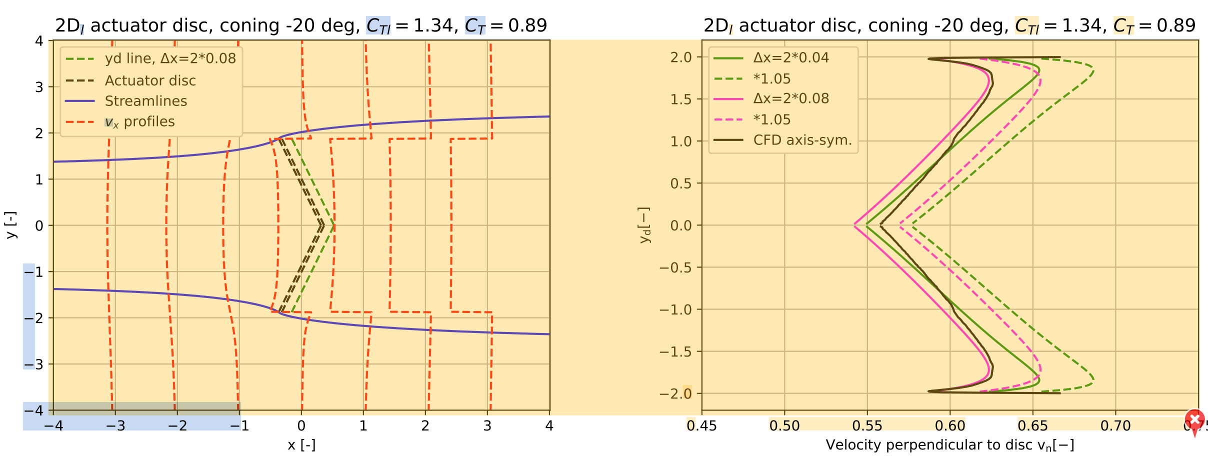

Figure 13. Same type of data as in Fig. 12 but for a cone angle of -20^o.

6.3 On the complexity of the flow solution for a coned disc

As mentioned in the introduction Crawford (2006) has proposed a correction to BEM for improving the modelling of a coned rotor. To illustrate with the present model how complex the induction is in a coned disc and thus how challenging a single point correction of BEM like the one of Crawford (2006) can be, we show in Fig. 14 the v_x and v_y contributions from both sides of the coned disc which then sums up to the total component. Disc 1 is the lower part of the downwind coned rotor and in the left graph in Fig. 14 the green line is thus the v_x induction from Disc 1 itself whereas the red line is the contribution from the other half part, Disc 2 of the coned rotor. This contribution is seen to be accelerated flow towards the center of the coned disc. Likewise we show the same for the v_y component in the graph to the right in Fig. 14. It's seen that the total component is about 0.4 at the tip and therefore contributes significantly to v_n. This illustrates the importance to include the radial component for the derivation of the induction in a coned rotor.

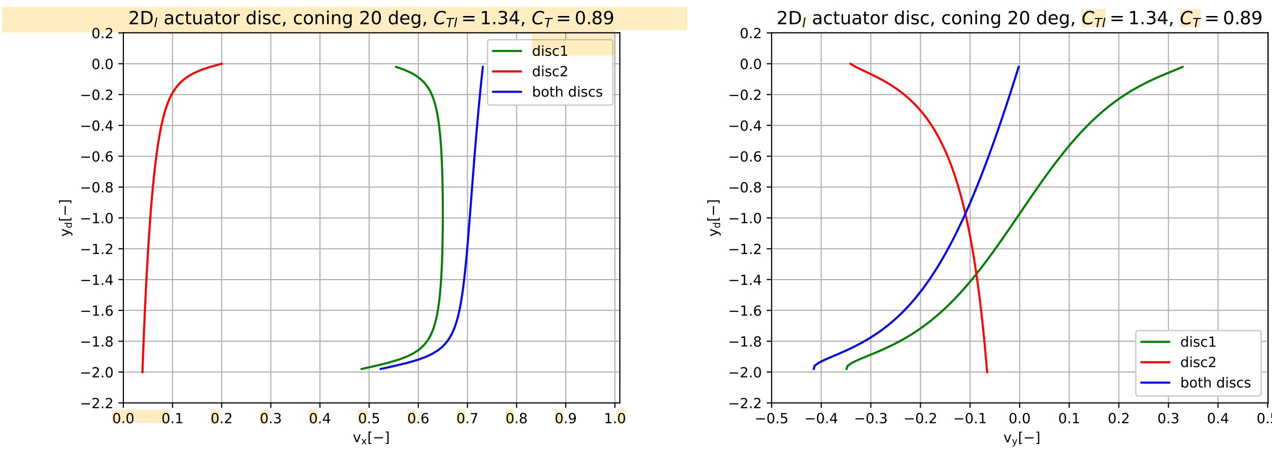

Figure 14. In the left graph we show the v_x components contributing to the total induction on the lower part, disc 1. The same for v_y in the graph to the right.

6.4 Flow solution for a range of cone angles

With the $2D_l$ model we have simulated the normal velocity, v_n, for a range of cone angles from 60^o to -60^o for a thrust coefficient of 0.89.

In Fig. 15 the graph to the left with the $v_n$result for positive cone angles we can see the shape of the profiles become more slender with an increasing difference in velocity at the center and at the edge. At low cone angles the increase in the normal velocity at the central part of the disc above the velocity for a plane disc can be noticed.

For the negative cone angles in the right graph of Fig. 15 the characteristic sweep on the outer part of the velocity profile towards higher induction can be seen up to a cone angle of about -40^o.

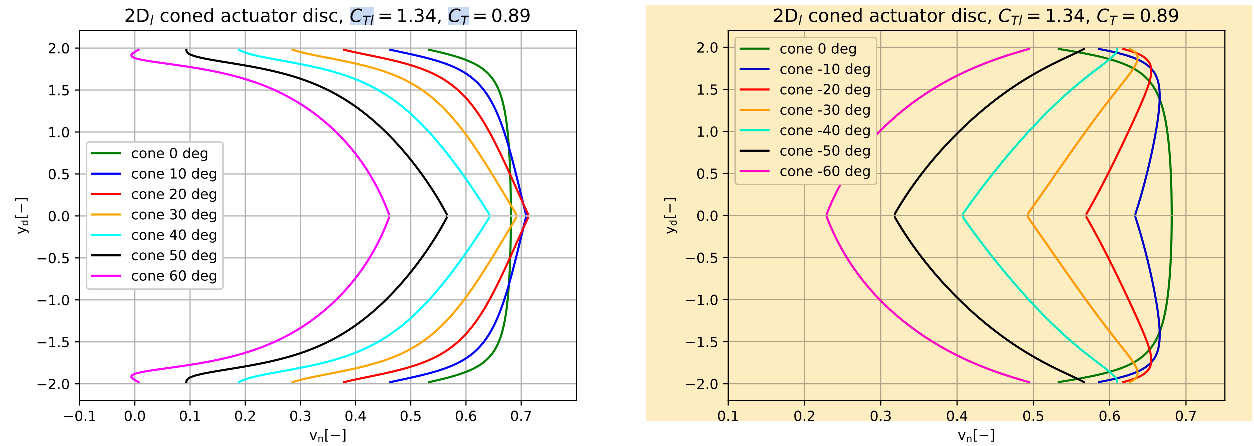

Figure 15. Simulated v_n distributions with the $2D_l$ model for a range of positive cone angles in the graph to the left and for negative cone angled to the right.

6.5 Coned disc in yaw

Finally, we have simulated a coned disc of 30^o in 20^o yawed flow to explore the capability of the $2D_l$ model to simulate such complex inflow. In the right graph in Fig. 16 we show the enclosing streamlines of the disc. A considerable downward deflection of the wake flow is seen. It means that a bigger part of the flow passing through the lower part of the disc is deflected outside the projected area of the disc and thus accelerated up to the free stream velocity due to the induced g forces.

In the right graph of Fig. 16 the normal velocity to the disc along the line yd parallel to the disc in a distance of $\Delta x = 2 \cdot 0.08$ shows as expected a jump passing through the center of the disc. Further it can be seen that the induction on the two sides of the yawed disc are quite different with a stronger variation from edge to center on the downwind part.

7 Outlook

The promising results of the $2D_l$ model based on comparisons with 3-D and axis-symmetric CFD simulations, respectively, indicate that although the model is two-dimensional it could form the basis for a consistent, general rotor induction model for wind turbine rotors with one equation for v_x and one for v_y including modelling of yawed and coned disc flow. This simplicity would also be of big advantage for the model to be used in rotor optimizations in the derivation of analytical gradients.

One prerequisite for the model to be used for a rotor induction model is a coupling to an angular momentum model for tangential induction. Following the model approach by Madsen et al. (2010) this can be done through the following equation derived from angular momentum balance over the actuator disc combined with a blade element analysis:

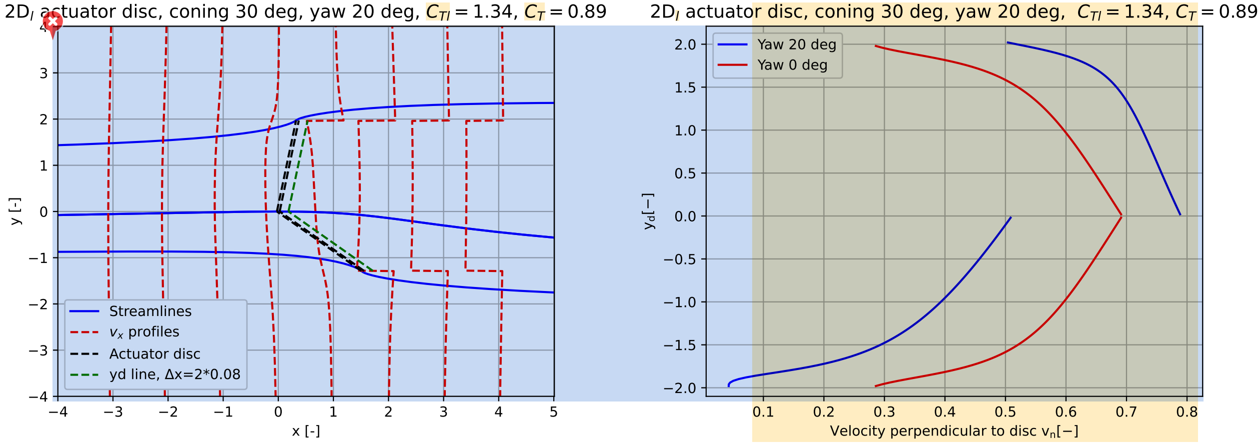

Figure 16. In the left graph we show the enclosing streamlines of a 30^o coned disc with a yaw angle of 20^o together with axial velocity profiles at different streamwise positions. In the graph to the right the normal velocity to the disc along the coned and yawed disc is shown in comparison withe the velocities for an aligned coned disc.

$$v_t = \frac{V_0 C_Q}{2(1-a)}, \tag{49}$$

where v_t is the tangential induced velocity and C_Q is the non-dimensional tangential load coefficient defined as:

$$C_Q = \frac{V_r^2 C_x c N_B}{V_0^2 2\pi r}, \tag{50}$$

and

$$C_x = C_l \sin\varphi - C_d \cos\varphi. \tag{51}$$

V_r is the relative velocity to the blade section, c local chord, N_B number of blades, φ the local flow angle from the rotor plane to V_r, c_l and c_d the local airfoil coefficients and a the axial induction factor which is computed with the $2D_l$ model. The specific implementation of the tangential induction model can be discussed, e.g. if its based on local values or probably best as the average C_Q and a over a ring element.

Likewise the input to the $2D_l$ model in form of C_T has to be derived from the blade element analysis and takes a similar form as for C_Q, (Madsen et al., 2010):

$$C_T = \frac{V_r^2 C_y c N_B}{V_0^2 2\pi r}, \tag{52}$$

with

$$C_y = C_l \cos\varphi + C_d \sin\varphi. \tag{53}$$

Further on the implementation of the $2D_l$ model in a rotor analysis, the induction should be computed along diagonal lines of the rotor using the local yaw/tilt angle and cone angle in the $2D_l$ model. Such implementation would fit well to the polar grid implementation of BEM in HAWC2 as described in Madsen et al. (2020). The approach could be computation of the induction along 12-16 diagonals at equally spaced azimuth positions which would give a good resolution of azimuthal variations due to non-uniform inflow and yaw/tilt angles.

It would also be necessary to relax on the constant loading assumed for the integration across the disc of Eq. 23 and 24. However, these integrals can be integrated numerically without slowing down the computations too much or as in the implementation of the Actuator Cylinder model (Madsen et al., 2013) where the loading is assumed to be piece wise constant which allows integration of influence coefficients only once in a time simulation.

The capability of the $2D_l$ model to simulate the flow through a coned rotor in yaw by using two yawed discs of different yaw angles with opposite sign is a big advantage of the model. This allows also for a straight forward simulation of a coned disc in yaw by yawing the one disc more than the other.

The superposition of several differently yawed discs with constant loading could also be used to approximate an arbitrary rotor shape and loading by a segmented diagonal line of discs just coinciding at the edges. This has some resemblance with the approach by Li et al. (2022) where a staggering of VC models shifted in streamwise direction is used to model non-planar rotors.

A final comment on the $2D_l$ model is that the evaluation of the velocities at a distance $5-10\%$ behind the disc means that the induction even for a plane rotor is not completely local as there would be velocity contributions from nearby points along the diagonal line. This is considered as an advantage as test cases with high loading in the aeroelastic code HAWC2 using the local induction approach indicate that some averaging of the local C_T should be used.

8 Conclusions

We have presented an analytical linear solution for a 2-D AD flow that is derived from the Euler equations and the equation of continuity. The induction at the disc is uniform for a constant loading like in the momentum theory but we have shown that immediately behind the disc the axial velocity profiles are non-linear and match by simple scaling a full non-linear axis-symmetric flow solution for an AD.

By a simple coordinate rotation the analytical solution was extended to a yawed disc. This flow solution matches well a full 3-D CFD simulation of a circular AD when comparing the normal velocity to the disc in the plane with skewed inflow up to $30-40^o$.

Superposition of more discs enabled studying turbine interaction and is also used to form a coned disc by positioning two yawed discs with opposite yaw angles so the edges of the discs just coincide. An excellent agreement for a downwind coned disc of 20^o was found when comparing the normal velocity to the disc with an axis-symmetric CFD simulation of a coned circular disc. For a disc with upwind coning of -20^o the typical shape of the velocity profile with increased induction on the most outboard part matched well the CFD simulations but some offset of the velocity profile was found.

The promising results of comparing the $2D_l$ model with 3-D and axis-symmetric CFD simulations on a circular AD have indicated that the $2D_l$ model could form the basis for a consistent, simple induction model for aerodynamic and aeroelastic wind turbine rotor simulations. First of all the model should for such application be combined with an angular momentum model which has been sketched in the paper. Then the computation of induction should be used along diagonal lines of the rotor in 12-16 different azimuth positions where the skewed inflow angle from yaw error or tilt is input to the model. Finally, an extension of the present implementation to simulate a variable loading across the disc could be done by numerical integration of the equations for v_x, v_y or by superposition of several yawed discs, each with a constant loading and yaw angle forming a segmented line approximating the real diagonal line of the rotor shape.

Code availability. The results from the $2D_l$ model have been simulated with different Python codes which are not well suited for sharing due to many temporary parts for output and other testing.

Data availability. The CFD simulations used for comparisons can be shared by contacting the author.

Code and data availability. See above.

Sample availability. Nothing.

Video supplement. Nothing.

Appendix A: Derivation of the pressure function

We show here the derivation of pressure potential for a 2-D disc or in fact an actuator strip extending from $-z$ to z and with doublets with the intensity Δp distributed over the surface S. For any point not situated on the disc the potential will according to Koning (1935) be given by:

$$p = \frac{1}{4\pi}\int_S \Delta p \frac{\partial}{\partial n}(\frac{1}{\omega})dS \tag{A1}$$

where n denotes the positive normal to the disc and ω the distance from any point on the disc to the point A where the potential is calculated. ω will then be:

$$\omega = \sqrt{x^2 + (y-\eta)^2 + \zeta^2} \tag{A2}$$

and insering in A1 we get:

$$p = \frac{1}{4\pi}\int_{-b}^{b} \Delta p d\eta \int_{-\infty}^{\infty} \frac{\partial}{\partial x}(\frac{1}{\sqrt{x^2+(y-\eta)^2+\zeta^2}})d\zeta = \frac{1}{4\pi}\int_{-b}^{b} \Delta p d\eta \int_{-\infty}^{\infty} \frac{-0.5\cdot 2x}{(x^2+(y-\eta)^2+\zeta^2)^{3/2}}d\zeta. \tag{A3}$$

The integral is of the type (207) in the handbook of Rumble (2023):

$$\int_{-\infty}^{\infty} \frac{dt}{T\sqrt{T}} = [\frac{2(2ct+b)}{q\sqrt{T}}\Bigg|_{-\infty}^{\infty}] \tag{A4}$$

where $T = a + bt + ct^2$ and $q = 4ac - b^2$

Now:

$a = x^2 + (y-\eta)^2$

$b = 0$

$c = 1$

$q = 4(x^2 + (y-\eta)^2))$

$T = x^2 + (y-\eta)^2 + t^2$

We integrate Eq. A3:

$$p = -\frac{1}{4\pi}\int_{-b}^{b} \Delta p d\eta \; [x\frac{2(2ct+b)}{q\sqrt{T}}\Bigg|_{-\infty}^{\infty} \tag{A5}$$

$$= -\frac{1}{4\pi}\int_{-b}^{b} \Delta p d\eta \, [x \frac{4t}{4[x^2+(y-\eta)^2]\sqrt{(x-\xi)^2+(y-\eta)^2+t^2}}\Bigg|_{-\infty}^{\infty} \tag{A6}$$

$$= -\frac{1}{4\pi}\int_{-b}^{b} \Delta p d\eta \, [\frac{x}{[x^2+(y-\eta)^2]} + \frac{x}{[(x-\xi)^2+(y-\eta)^2]}] \tag{A7}$$

$$= -\frac{1}{2\pi}\int_{-b}^{b} \Delta p \frac{x}{x^2+(y-\eta)^2} d\eta. \tag{A8}$$

Appendix B: Derivation of the velocity component w_y pressure function

The starting point is Eq. 12 with the volume forces $f_y, g_y = 0$:

$$\frac{\partial w_y}{\partial x} = -\frac{\partial p}{\partial y} \tag{B1}$$

and thus:

$$w_y = \int_{-\infty}^{x} \frac{\partial w_y}{\partial x} dx = -\int_{-\infty}^{x} \frac{\partial p_y}{\partial y} dx. \tag{B2}$$

We differentiate the pressure Eq. A8 with respect to y:

$$\frac{\partial p}{\partial y} = -\frac{1}{2\pi}\int_{-1}^{1} \Delta p \frac{-2(y-\eta)x}{x^2+(y-\eta)^2} d\eta. \tag{B3}$$

Inserting Eq. B3 into Eq. B2:

$$w_y = \frac{1}{2\pi}\int_{-1}^{1} 2(y-\eta)\Delta p d\eta \int_{-\infty}^{x} \frac{x}{x^2+(y-\eta)^2} dx. \tag{B4}$$

For the integration of the last integral in Eq. B4 we note the integral is of the type (113) in the handbook of Rumble (2023):

$$\int \frac{t}{T} = \frac{2a+bt}{qT} - \frac{b}{q}\int \frac{dt}{T} \tag{B5}$$

where: $T = a + bt + ct^2$

We have:

$T = t^2 + (y-\eta)^2$

$a = (y-\eta)^2$

$b = 0$

$c = 1$

$q = 4ac - b^2 = 4(y-\eta)^2$

$$w_y = \frac{1}{2\pi}\int\limits_{-1}^{1} 2(y-\eta)\Delta p d\eta \cdot \left[\frac{2a)}{qT}\right]\Bigg|_{-\infty}^{x} = \frac{1}{2\pi}\int\limits_{-1}^{1} 2(y-\eta)\Delta p d\eta \cdot \frac{2(y-\eta)^2}{(4(y-\eta)^2)(x^2+(y-\eta)^2)} \tag{B6}$$

$$w_y = \frac{1}{2\pi}\int\limits_{-1}^{1} \Delta p \frac{(y-\eta)}{(x^2+(y-\eta)^2)} d\eta. \tag{B7}$$

Appendix C: Derivation of the pressure function for constant loading

The pressure function has in Eq. A8 been derived to:

$$p = -\frac{1}{2\pi}\int\limits_{-1}^{1} \Delta p \frac{x}{x^2+(y-\eta)^2} d\eta. \tag{C1}$$

When the loading Δp is constant we can derive the analytical solution for the pressure.
The integral is of the type (107) in the handbook of Rumble (2023):

$$\int \frac{dt}{T} = \frac{2}{\sqrt{q}} \arctan \frac{2ct+b}{\sqrt{q}} \tag{C2}$$

where: $T = a + bt + ct^2$.

We have:

$T = t^2 - 2yt + (x^2 + y^2)$

$a = x^2 + y^2$

$b = -2y$

$c = 1$

$q = 4ac - b^2 = 4(x^2 + y^2) - (-2y)^2$

$\sqrt{q}$ = 2x

$$p = -\frac{1}{2\pi} x\Delta p\,[\frac{2}{2x}\arctan(\frac{2t-2y)}{2x})]\Bigg|_{-1}^{1} = -\frac{1}{2\pi} x\Delta p\,[\frac{2}{2x}\arctan(\frac{2-2y)}{2x} - \arctan(\frac{-2-2y)}{2x}] \tag{C3}$$

$$p = -\frac{1}{2\pi}\Delta p[\arctan(\frac{1-y)}{x} + \arctan(\frac{1+y)}{x}]. \tag{C4}$$

Appendix D: Derivation of w_y for a constant loading

w_y has in Eq. 24 been derived to:

$$w_y = \frac{1}{2\pi}\int_{-1}^{1} \Delta p \frac{y-\eta}{x^2 + (y-\eta)^2} d\eta. \tag{D1}$$

The integral is of the type (112) in the handbook of Rumble (2023):

$$-\int \frac{dt \cdot t}{T} = -\frac{1}{2c}\ln T + \frac{b}{2c}\int \frac{dt}{T} \tag{D2}$$

and (107):

$$y\int \frac{dt}{T} \tag{D3}$$

where: $T = a + bt + ct^2$

and

$T = t^2 - 2yt + (x^2 + y^2)$

$a = x^2 + y^2$

$b = -2y$

$c = 1$

$q = 4ac - b^2 = 4(x^2 + y^2) - (-2y)^2 = 4x^2$
$\sqrt{q} = 2x$

We first notice that the last integral in D2 cancels with the integral in D3 as we have:

$$\frac{b}{2c}\int \frac{dt}{T} = \frac{-2y}{2}\int \frac{dt}{T} = -y\int \frac{dt}{T}. \tag{D4}$$

(D5)

For the other integral in D2 when inserting into Eq D1 we have:

$$w_y = -\frac{1}{2\pi}\Delta p\,[\frac{1}{2}\ln(t^2 - 2yt + (x^2 + y^2))]\Big|_{-1}^{1} \; => \tag{D6}$$

$$w_y = \frac{1}{4\pi}\Delta p[\ln(1 - 2y + (x^2 + y^2)) - \ln(1 + 2y + (x^2 + y^2))] => \tag{D7}$$

$$w_y = -\frac{1}{4\pi}\Delta p[\ln(\frac{x^2 + (y+\eta)^2}{x^2 + (y-\eta)^2}). \tag{D8}$$

Author contributions. HAM has done all the model development, written the Python codes to simulate the $2D_l$ model, carried out the CFD computations back in time and written the paper.

Competing interests. The author declares that he has no conflict of interest.

Disclaimer. None.

Acknowledgements. Thanks to Kenneth Thomsen, Head of division "Wind Turbine Design" in Department "Wind and Energy Systems" at DTU and to Professor Christian Back, head of section "ARD", in Department "Wind and Energy Systems" at DTU, for providing internal funding for this work.
Thanks also to Special Consultant Flemming Rasmussen in section "ARD", DTU Wind and Energy Systems, for carrying out a pre-review. Likewise the pre-review of the paper by Mads Holst Aagaard Madsen, postdoc at the Technical University of Munich is acknowledged.
Finally, thanks to the reviewer #1 David Wood and anonymous reviewer #2 for their valuable input.
And thanks to Jaime Liew at MIT for drawing attention to a few typos in the equations.

References

Boorsma, K., Schepers, G., Aagard Madsen, H., Pirrung, G., Sørensen, N., Bangga, G., Imiela, M., Grinderslev, C., Meyer Forsting, A., Shen, W. Z., Croce, A., Cacciola, S., Schaffarczyk, A. P., Lobo, B., Blondel, F., Gilbert, P., Boisard, R., Höning, L., Greco, L., Testa, C., Branlard, E., Jonkman, J., and Vijayakumar, G.: Progress in the validation of rotor aerodynamic codes using field data, Wind Energy Science, 8, 211–230, https://doi.org/10.5194/wes-8-211-2023, 2023.

Bortolotti, P., Kapila, A., and Bottasso, C. L.: Comparison between upwind and downwind designs of a 10thinsp;MW wind turbine rotor, Wind Energy Science, 4, 115–125, https://doi.org/10.5194/wes-4-115-2019, 2019.

Bortolotti, P., Ivanov, H., Johnson, N., Barter, G. E., Veers, P., and Namura, N.: Challenges, opportunities, and a research roadmap for downwind wind turbines, Wind Energy, 25, 354–367, https://doi.org/10.1002/we.2676, 2022.

Bossanyi, E.: GH Bladed Theory Manual. Technical Report, GH & Partners Ltd, Bristol, United Kingdom,, 2003.

Botasso, C. and Croce, A.: Cp-Lambda: Users Manual. Milano: Dipartimento di Ingegneria Aerospaziale, Polytecnico di Milano, 2006-2013.

Branlard, E. and Gaunaa, M.: Cylindrical vortex wake model: right cylinder, Wind Energy, 18, 1973–1987, https://doi.org/10.1002/we.1800, 2015.

Crawford, C.: Re-examining the precepts of the blade element momentum theory for coning rotors, Wind Energy, 9, 457–478, https://doi.org/10.1002/we.197, 2006.

Gaunaa, M., Troldborg, N., and Branlard, E.: A simple vortex model applied to an idealized rotor in sheared inflow, Wind Energy Science, 8, 503–513, https://doi.org/10.5194/wes-8-503-2023, 2023.

Glauert, H.: Airplane Propellers, in: Division L in Aerodynamic Theory, vol. IV, Durand WF (ed.)., pp. 169–360, Springer, 1935.

Jonkman, J., Hayman, G., Jonkman, B., and Damiani, R.: AeroDyn v15 User's Guide and Theory Manual, NREL, 2016.

Koning, C.: Influence of the Propeller on Other Parts of the Airplane Structure, Aerodynamic Theory, pp. 361–430, https://doi.org/10.1007/978-3-642-91487-4_4, 1935.

Larsen, T. and Hansen, A.: How 2 HAWC2, the user's manual, Denmark. Forskningscenter Risoe. Risoe-R-1597, 2007.

Li, A., Gaunaa, M., Pirrung, G. R., and Horcas, S. G.: A computationally efficient engineering aerodynamic model for non-planar wind turbine rotors, Wind Energy Science, 7, 75–104, https://doi.org/10.5194/wes-7-75-2022, 2022.

Madsen, H. A.: The actuator cylinder :, Institute of Industrial Constructions and Energy Technology, Aalborg University Centre,, 1982.

Madsen, H. A.: On the ideal and real energy conversion in a straight bladed vertical axis wind turbine, Phd thesis, Aalborg University, 1983.

Madsen, H. A.: Actuator Cylinder: A Flow Model for Vertical Axis Wind Turbine, Proceedings of the BWEA Wind Energy Conference (british Wind Energy Association), pp. 147–154, 1985.

Madsen, H. A.: Application of Actuator Surface Theory on Wind Turbines, in: IEA R&D WECS: Joint action on aerodynamics of wind turbines, 1988.

Madsen, H. A.: Forskning i aeroelasticitet EFP-2000, Chapter 6 Yawberegning i HAWC, p. 110 s., 2001.

Madsen, H. A. and Rasmussen, F.: The influence on energy conversion and induction from large blade deflections, Wind Energy for the Next Millennium. Proceedings, pp. 138–141, 1999.

Madsen, H. A., Bak, C., Døssing, M., Mikkelsen, R. F., and Øye, S.: Validation and modification of the Blade Element Momentum theory based on comparisons with actuator disc simulations, Wind Energy, 13, 373–389, https://doi.org/10.1002/we.359, 2010.

Madsen, H. A., Larsen, T. J., Schmidt Paulsen, U., and Vita, L.: Implementation of the Actuator Cylinder Flow Model in the HAWC2 code for Aeroelastic Simulations on Vertical Axis Wind Turbines, Proceedings of 51st Aiaa Aerospace Sciences Meeting Including the New Horizons Forum and Aerospace Exposition, pp. 12 pp., 12 pp., 2013.

Madsen, H. A., Larsen, T. J., Pirrung, G., Li, A., and Zahle, F.: Implementation of the Blade Element Momentum Model on a Polar Grid and its Aeroelastic Load Impact, Wind Energy Science, 5, 1–27, https://doi.org/10.5194/wes-2019-53, 2020.

Madsen, H. Aa.: Yaw simulation using a 3D actuator disc model coupled to the aeroelastic code HawC, In IEA Joint Action. Aerodynamics of Wind Turbines. 13. Symposium, Stockholm, 29–30 Nov 1999., pp. 133–145, 2000.

Madsen, H. A.: A CFD analysis of the actuator disc flow compared with momentum theory results, pp. 109–124, 1997.

Mikkelsen, R. F., Sørensen, J. N., and Shen, W. Z.: Modelling and analysis of the flow field around a coned rotor, Wind Energy, Vol. 4, 2001.

Øye, S.: FLEX4 simulation of wind turbine dynamics. Proceedings of the 28th IEA Meeting of Experts Concerning State of the Art of Aeroelastic Codes for Wind Turbine Calculations, Lyngby, Denmark. Edited by B. Maribo Pedersen, 1996.

Pao, L. Y., Zalkind, D. S., Griffith, D. T., Chetan, M., Selig, M. S., Ananda, G. K., Bay, C. J., Stehly, T., and Loth, E.: Control co-design of 13 MW downwind two-bladed rotors to achieve 25

Riziotis, V. and Voustinas, S.: Gast: A General Aerodynamic and Structural Prediction Tool for Wind Turbines. In Proceedings of the EWEC'97. Dublin, Ireland., 1997.

Rumble, John R., e.: CRC Handbook of Chemistry and Physics, 104th Edition (Internet Version 2023), CRC Press/Taylor Francis, Boca Raton, FL., 2023.

Sørensen, J. N. and Kock, C. W.: A model for unsteady rotor aerodynamics, Journal of Wind Engineering and Industrial Aerodynamics, 58, 259–275, https://doi.org/10.1016/0167-6105(95)00027-5, 1995.

Troldborg, N., Sørensen, J. N., Mikkelsen, R., and Sørensen, N.: A simple atmospheric boundary layer model applied to large eddy simulations of wind turbine wakes, Wind Energ., 17, 657–669, https://doi.org/10.1002/we.1608, 2014.

van Bussel, G.: The use of the asymptotic acceleration potential method for horizontal axis wind turnime rotor aerodynamics, Journal of Wind Engineering and Industrial Aerodynamics, 39, 161–172, https://doi.org/10.1016/0167-6105(92)90542-I, 1992.

van Kuik, G. A. and Lignarolo, L. E.: Potential flow solutions for energy extracting actuator disc flows, Wind Energy, 19, 1391–1406, https://doi.org/10.1002/we.1902, 2016.

Von Kármán, T. and Burgers, J.: Aerodynamic Theory: General aerodynamic theory : Perfect fluids / [By] Th. von Kármán ; J. M. Burgers, vb. 2, J. Springer, https://books.google.dk/books?id=RC0HaAEACAAJ, 1935.

Vølund, P. and Rasmussen, F.: Designverifikation for fleksibel to-bladet mølle, 1999.

WMC: FOCUS6 - The integrated wind turbine design suite, Knowledge Centre WMC, 2019.

Wood, D. H. and Hammam, M. M.: Optimal performance of actuator disc models for horizontal-axis turbines, Frontiers in Energy Research, 10, 971 177, https://doi.org/10.3389/fenrg.2022.971177, 2022.